Enhancing galloping-based energy harvesting through expanded quasi-zero-stiffness region

OPEN ACCESS
IOP Publishing
Smart Materials and Structures
Smart Mater. Struct. **34** (2025) 055018 (15pp)
https://doi.org/10.1088/1361-665X/add3db

Enhancing galloping-based energy harvesting through expanded quasi-zero-stiffness region

Chunbo Lan[1], Ye Zhang[2], Shuo Wang[1], Yang Lu[1], Yawei Wang[2] and Guobiao Hu[2,*]

[1] National Key Laboratory of Helicopter Aeromechanics, Nanjing University of Aeronautics and Astronautics, Nanjing 210016, People's Republic of China
[2] Internet of Things Thrust, The Hong Kong University of Science and Technology (Guangzhou), Guangzhou, Guangdong 511400, People's Republic of China

E-mail: guobiaohu@hkust-gz.edu.cn

Received 25 January 2025, revised 27 March 2025
Accepted for publication 1 May 2025
Published 14 May 2025

Abstract

In recent years, quasi-zero-stiffness (QZS) structures have been utilized in designing galloping piezoelectric energy harvesters (GPEHs) to produce large vibration responses and high output power. However, the QZS region is relatively narrow, leading to limited enhancement of QZS-GPEH at large displacement responses. To address this issue, this paper proposes a flat potential-well tuning method to design an improved QZS-GPEH (IQZS-GPEH) by significantly expanding the QZS region. First, the governing equations of the proposed IQZS-GPEH were derived, and a static analysis was conducted to compare the QZS region of the IQZS-GPEH with that of a conventional QZS-GPEH. The results reveal that the QZS property can be extended to accommodate large displacement responses, remarkably expanding the QZS region. Subsequently, the harmonic balance method was applied to derive approximate analytical solutions, and numerical simulations were performed to verify and study the dynamics and power performance of the GPEHs. Finally, wind tunnel experiments were conducted to validate the theoretical and numerical findings. The results show that the proposed method effectively enlarges the QZS region, substantially increasing dynamic responses and voltage outputs. Specifically, as the wind speed increased from 3.6 m s^{-1} to 5.0 m s^{-1}, the power output improvement rose from 23.55% to 55.64%. Therefore, it can be concluded that broadening the QZS region is an effective approach to enhancing the performance of QZS-based galloping energy harvesters.

Keywords: galloping, piezoelectric energy harvesting, quasi-zero-stiffness, nonlinear dynamics

* Author to whom any correspondence should be addressed.

1. Introduction

In recent years, the rapid development of wireless sensors has led to a significant increase in the widespread application of low-power, small-scale devices. To address the scattered power demands of these distributed devices, various energy harvesting technologies [1–3], including vibration energy harvesting, ocean energy harvesting, and wind energy harvesting, have been developed.

To efficiently harvest low-speed wind energy, like breezes, mechanisms of flow-induced vibrations, including galloping [4], flutter [5], and vortex-induced vibration [6], have been extensively exploited in designing small-scale wind energy harvesters. Among these, galloping-based wind energy harvesters are highly favored for their large structural responses characterized by limit-cycle oscillations. Once the wind speed exceeds the cut-in wind speed, a galloping energy harvester can produce a significant response and generate high power output. The concept of the galloping energy harvester was first proposed and demonstrated by Barrero-Gil *et al* [7] and Sirohi and Mahadik [8]. Their galloping energy harvester consists of a piezoelectric cantilever beam and a bluff body attached at its free end. When the wind interacts with the bluff body, an aerodynamic force is generated that induces the vibration of the piezoelectric beam, thereby producing power output. Piezoelectric materials are commonly employed in the design of wind energy harvesters, primarily due to their lightweight, high power density, and ease of integration [2].

Obviously, a large structural response leads to a significant increase in voltage. Therefore, optimizing the structural design is essential for enhancing output power. From this perspective, researchers have devoted considerable effort to designing bluff bodies and host structures. For instance, early studies explored and compared bluff bodies with different cross-sectional shapes [9–11], including triangular, D-shaped, and square sections for wind energy harvesting. Results revealed that the square section configuration exhibits superior performance compared to other geometries [11]. Subsequently, bluff body design has become a primary method for improving wind energy harvesting performance, with the shapes of bluff bodies becoming increasingly diverse [12–14].

Besides bluff body design, the piezoelectric structure that hosts the bluff body also affects energy harvesting performance. The cut-in wind speed is closely related to structural damping, while the maximum structural response depends on structural stiffness, tip mass, and damping. Inspired by the significant success of applying nonlinearity in vibration energy harvesting, researchers have explored nonlinearity [15–24] as a promising approach to increase structural response and reduce cut-in wind speed for galloping piezoelectric energy harvesters (GPEHs).

A pioneering study by Bibo *et al* [15] introduced nonlinear stiffness into a conventional cantilever-beam-based GPEH using magnets. Their results demonstrated that high-energy orbit oscillations in both monostable and bistable GPEHs could enhance structural responses and power outputs within a specific wind speed range. Subsequently, Wang *et al* [16] proposed a tristable GPEH by modifying the magnet arrangement, and experimental results showed that a maximum power output of 0.73 mW was achieved at a wind speed of 7.0 m s^{-1}. Zhao and Yang [17] incorporated an impact mechanism into GPEHs and found that at a wind speed of 5.5 m s^{-1} and a base acceleration of 0.5 g, the output power increased from 3.0 mW to 3.8 mW. Furthermore, Zhao *et al* [18] experimentally tested a nonlinear 2-DOF GPEH with a cut-out cantilever beam as its host structure and found that this nonlinear GPEH had an exceptionally low cut-in wind speed of 1 m s^{-1}.

To understand the underlying mechanism, Lan *et al* [19] theoretically studied a 2-DOF GPEH and derived approximate solutions. They found that the cut-in wind speed of a 2-DOF GPEH is closely related to both structural damping and stiffness, whereas the cut-in wind speed of a conventional SDOF GPEH depends solely on structural damping. Therefore, properly tuning the stiffness of a 2-DOF GPEH can reduce the cut-in wind speed, which is beneficial for low-speed wind energy harvesting. Building on a similar concept, Yang *et al* [20] developed a magnetically coupled dual-beam GPEH and reduced cut-in wind speed by up to 41.9%. Sun *et al* [21] proposed a tandem configuration of magnetically coupled 2-DOF GPEHs and achieved a 65% improvement in power output.

More recently, Chen and Zhao [22] utilized a quasi-zero-stiffness (QZS) structure to design a GPEH. The QZS structure, characterized by high static stiffness and very low dynamic stiffness, is widely used in ultra-low-frequency vibration isolation. It has been demonstrated that the QZS structure can generate large responses due to its nearly zero (i.e. quasi-zero) dynamic stiffness near the static equilibrium position. However, the QZS range for this GPEH is pretty limited, resulting in no significant structural response improvement at high wind speeds. To overcome this limitation, this paper proposes a novel method that utilizes nonlinear positive stiffness to counterbalance nonlinear negative stiffness, thus expanding the quasi-zero-stiffness range. The content of this paper is organized as follows: section 2 introduces the design method for achieving an ultra-wide QZS range and presents the governing equations of the proposed system. Section 3 applies the harmonic balance method (HBM) to derive the approximate analytical solutions, followed by a comprehensive assessment of the wind energy harvesting performance. Section 5 presents experimental test results to validate the conclusions obtained from the theoretical analysis.

2. Design of a magnetically quazi-zero-stiffness GPEH

2.1. Ultra-wide QZS range design method

A conventional QZS galloping energy harvester QZS-GPEH, as illustrated in figure 1(a), comprises a piezoelectric beam, a bluff body attached to its free end, and a pair of magnets producing repulsive forces. These magnets provide negative stiffness within a specific displacement range, counterbalancing the positive stiffness of the piezoelectric beam. By appropriately adjusting the magnet distance, the equivalent stiffness of the entire system can be made zero at $x = 0$.

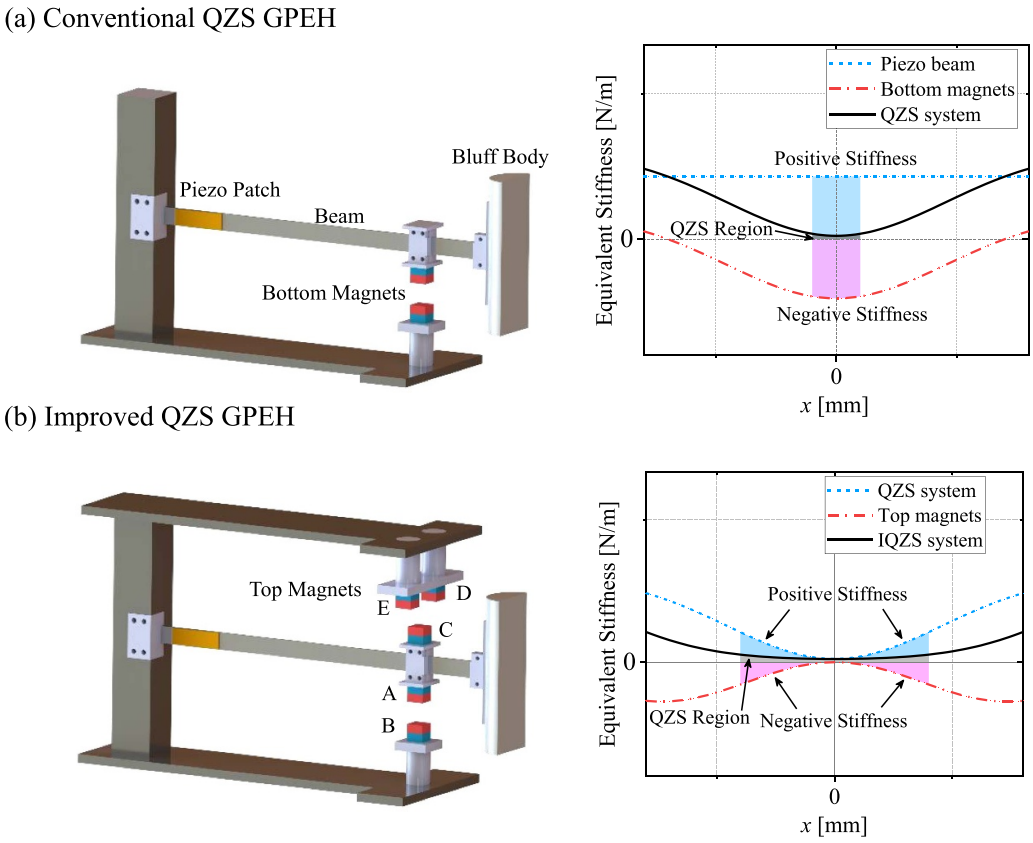

Figure 1. Illustration of the two configurations of quasi-zero-stiffness galloping piezoelectric energy harvester: (a) QZS-GPEH, (b) IQZS-GPEH.

This method is commonly used to achieve a QZS system, which exhibits an exceptionally low resonant frequency compared to its linear counterpart. Consequently, the displacement response of the QZS system is typically much larger than the linear ones. When the galloping phenomenon is induced, the large displacement response, resulting from the QZS feature, significantly enhances the power output of the piezoelectric transducer. This constitutes the primary advantage of the QZS-GPEH. However, conventional QZS-GPEHs' QZS ranges are relatively narrow, meaning that the equivalent stiffness increases rapidly with the displacement response. To fully leverage the benefits of QZS, it is essential to broaden its range.

To this end, this paper proposes an improved QZS (IQZS) GPEH (IQZS-GPEH) with an extended QZS range. Figure 1 shows the structure of the proposed IQZS-GPEH and compares its QZS feature with that of a conventional QZS-GPEH. The main distinction between these two systems lies in the specifically designed magnet configuration. The proposed system utilizes five magnets, whereas the conventional one uses two. The detailed magnet configuration is depicted in figure 2. The bottom two magnets (Magnets A and B, with a vertical distance of D_0) follow the same configuration as in the conventional setup. The top three magnets have a different arrangement. Specifically, Magnet C is mounted above the piezoelectric beam, while Magnets D and E are positioned on the two sides. The vertical and horizontal distances between these magnets are D_1 and s, respectively. This arrangement of magnets generates the negative stiffness to balance the positive stiffness at large displacements, thereby achieving QZS over a wide range. Additionally, the equivalent stiffness near $x = 0$ remains close to zero due to the presence of the three top magnets. Consequently, by incorporating these top magnets into the setup of a conventional QZS-GPEH, QZS can be achieved at both small and large displacements, significantly expanding its effective range.

2.2. *Mathematical modeling*

Based on the linear assumption of electromechanical coupling and elastic behavior, the lumped parameter model [15–19] of a GPEH that consists of a piezoelectric beam with a bluff body at its free end has been maturely developed and widely utilized. Based on this lumped parameter model, the governing equations of the proposed GPEH can be written as

$$\begin{cases} M\ddot{x} + C\dot{x} + Kx + F_m + F_a - \theta v = 0 \\ \theta\dot{x} + C_p\dot{v} + \dfrac{v}{R} = 0 \end{cases} \tag{1}$$

where M, C, and K are, respectively, the equivalent mass, damping coefficient, and stiffness of the GPEH. θ is the electromechanical coupling coefficient; C_{pp} is the clamped capacitance of the piezoelectric patch; x is the

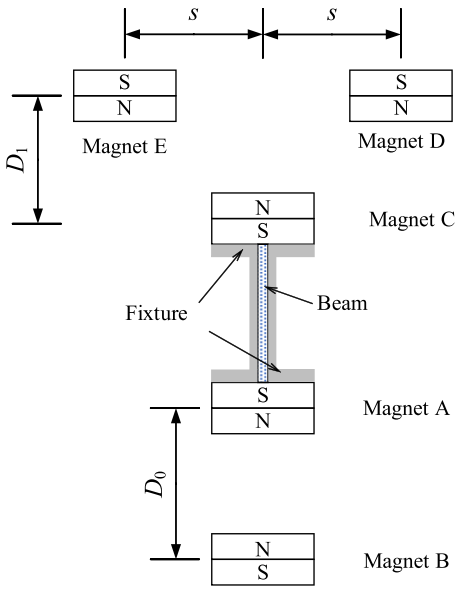

Figure 2. Magnets configuration for the proposed IQZS-GPEH.

displacement of the bluff body relative to the base; v is the output voltage of the piezoelectric patch; F_{m} is the force induced by magnetic interactions; F_{a} is the horizontal component of the aerodynamic force acting on the bluff body.

To obtain the aerodynamic force, the quasi-steady assumption [25], in which the motion of the bluff body is very slow compared to the motion of the wind, is employed. Under the quasi-steady assumption, the aerodynamic force coefficients keep constant for a given angle of attack. Therefore, the aerodynamic force F_{a} can be represented by

$$F_{\mathrm{a}} = \frac{1}{2}\rho LDU^2\left[s_1\frac{\dot{x}}{U} - s_3\left(\frac{\dot{x}}{U}\right)^3\right] \tag{2}$$

where L and D are the length and width of the bluff body. ρ is the air density; U is the wind speed; s_1 and s_3 are the empirical linear and cubic coefficients of the transverse galloping force, which can be determined through CFD simulations.

To calculate the magnetic interaction force, the dipole-dipole model is employed. Therefore, the potential energy induced by Magnets A and B is

$$\begin{aligned} U_{\mathrm{bottom}} &= -\frac{\mu_0}{4\pi}\left[\frac{1}{\|r_{BA}\|_2^3}\boldsymbol{m_B} - 3\frac{\boldsymbol{m_B}\cdot r_{BA}}{\|r_{BA}\|_2^5}r_{BA}\right]\cdot\boldsymbol{m_B} \\ &= -\frac{\mu_0 M_A V_A M_B V_B}{4\pi}\left[\frac{1}{\left(x^2+D_0^2\right)^{3/2}} - \frac{3D_0^2}{\left(x^2+D_0^2\right)^{5/2}}\right] \end{aligned} \tag{3}$$

where μ_0 is the vacuum permeability; $\boldsymbol{m_A}$ and $\boldsymbol{m_B}$ are magnetic moment vectors of magnets A and B; $\boldsymbol{r}_{\mathrm{BA}}$ is the vector from the center of magnet to that of magnet B; $\|\,\|_2$ is the L2-norm; M_A and M_B are the magnitudes of $\boldsymbol{m_A}$ and $\boldsymbol{m_B}$; V_A and V_B are the volumes of magnets A and B.

For simplicity, all these magnets used in this paper share the same size and magnetic properties, e.g. $M_A = M_B = M_0$, $V_A = V_B = V_0$. Hence, we can define the below coefficient:

$$\lambda = \frac{\mu_0 M_0^2 V_0^2}{4\pi}. \tag{4}$$

The potential energy induced by the top three magnets is

$$U_{\mathrm{Top}} = -\lambda\left[\frac{1}{\left((x+s)^2+D_1^2\right)^{3/2}} - \frac{3D_1^2}{\left((x+s)^2+D_1^2\right)^{5/2}} + \frac{1}{\left((x-s)^2+D_1^2\right)^{3/2}} - \frac{3D_1^2}{\left((x-s)^2+D_1^2\right)^{5/2}}\right]. \tag{5}$$

Thus, the overall energy induced by the five magnets can be obtained as

$$\begin{aligned} U_m &= U_{\mathrm{bottom}} + U_{\mathrm{top}} \\ &= -\lambda\left[\begin{array}{l} \frac{1}{\left(x^2+D_0^2\right)^{3/2}} - \frac{3D_0^2}{\left(x^2+D_0^2\right)^{5/2}} + \frac{1}{\left((x+s)^2+D_1^2\right)^{3/2}} - \frac{3D_1^2}{\left((x+s)^2+D_1^2\right)^{5/2}} \\ + \frac{1}{\left((x-s)^2+D_1^2\right)^{3/2}} - \frac{3D_1^2}{\left((x-s)^2+D_1^2\right)^{5/2}} \end{array}\right]. \end{aligned} \tag{6}$$

Then, the magnetic force can be derived from equation (6), yielding

$$\begin{cases} F_m = F_{\text{bottom}} + F_{\text{top}} \\ F_{\text{bottom}} = -\lambda\left[-\dfrac{3x}{\left(x^2+D_0^2\right)^{5/2}} + \dfrac{15xD_0^2}{\left(x^2+D_0^2\right)^{7/2}}\right] \\ F_{\text{top}} = -\lambda\left[-\dfrac{3\left(x+s\right)}{\left(\left(x+s\right)^2+D_1^2\right)^{5/2}} + \dfrac{15\left(x+s\right)D_1^2}{\left(\left(x+s\right)^2+D_1^2\right)^{7/2}} - \dfrac{3\left(x-s\right)}{\left(\left(x-s\right)^2+D_1^2\right)^{5/2}} + \dfrac{15\left(x-s\right)D_1^2}{\left(\left(x-s\right)^2+D_1^2\right)^{7/2}}\right] \end{cases}. \tag{7}$$

Substituting equations (2) and (7) back into equation (1), the governing equations of the proposed IQZS-GPEH can be obtained as

$$\begin{cases} M\ddot{x} + C\dot{x} + Kx + F_{\text{bottom}} + F_{\text{top}} + \dfrac{1}{2}\rho LDU^2\left[s_1\dfrac{\dot{x}}{U} - s_3\left(\dfrac{\dot{x}}{U}\right)^3\right] - \theta v = 0 \\ \theta\dot{x} + C_p\dot{v} + \dfrac{v}{R} = 0 \end{cases}. \tag{8}$$

If the three magnets on the top side are removed, the system degrades to a conventional QZS-GPEH, and the governing equations become

$$\begin{cases} M\ddot{x} + C\dot{x} + Kx - \lambda\left[-\dfrac{3x}{\left(x^2+D_0^2\right)^{5/2}} + \dfrac{15xD_0^2}{\left(x^2+D_0^2\right)^{7/2}}\right] + \dfrac{1}{2}\rho LDU^2\left[s_1\dfrac{\dot{x}}{U} - s_3\left(\dfrac{\dot{x}}{U}\right)^3\right] - \theta v = 0 \\ \theta\dot{x} + C_p\dot{v} + \dfrac{v}{R} = 0 \end{cases}. \tag{9}$$

2.3. Static analysis

For the conventional QZS GPEH, the system stiffness is zero when $x = 0$. From equation (9), it is learned that at static equilibrium, the system stiffness is

$$K - \lambda\left[-\frac{3}{\left(x^2+D_0^2\right)^{5/2}} + \frac{15D_0^2}{\left(x^2+D_0^2\right)^{7/2}}\right] = 0. \tag{10}$$

Equation (10) suggests the condition for the magnetic distance D_0 to satisfy the QZS requirement. To showcase the IQZS characteristics, a comparison was made between the proposed IQZS system and the conventional counterpart using the parameters listed in table 1. Figure 3 shows the potential energy, restoring force, and equivalent stiffness of a traditional QZS system. It is noted in figure 3(c) that the negative stiffness attributed to the magnetic force counterbalances the positive stiffness generated by the piezoelectric beam near $x = 0$. As a result, the potential energy near $x = 0$ is flat (figure 3(a)), and the equivalent stiffness is almost zero.

Inspired by the flat potential well, the novel methodology to achieve QZS no longer relies on the zero-stiffness design. Instead, it focuses on designing a flat potential well over a wide range. Figure 4 illustrates the potential energy, restoring force, and equivalent stiffness of the proposed IQZS system. First, the bottom two magnets and the piezoelectric beam form a typical monostable potential shape. The height of the potential energy at $x = d$ is

$$\begin{aligned} \Delta U_{\text{bottom}} &= \left[U_{\text{bottom}}\left(x=d\right) + U_{\text{beam}}\left(x=d\right)\right] \\ &\quad - \left[U_{\text{bottom}}\left(x=0\right) + U_{\text{beam}}\left(x=0\right)\right] \\ &= -\frac{\mu_0 M_A V_A M_B V_B}{4\pi} \\ &\quad \times\left[\frac{1}{\left(d^2+D_0^2\right)^{3/2}} - \frac{3D_0^2}{\left(d^2+D_0^2\right)^{5/2}} + \frac{2}{D_0^3}\right] + Kd^2. \end{aligned} \tag{11}$$

Meanwhile, the height of the potential energy generated by the top three magnets at $x = d$ is

$$\begin{aligned} \Delta U_{\text{top}} &= U_{\text{top}}\left(x=d\right) - U_{\text{top}}\left(x=0\right) \\ &= -\lambda\left[\frac{1}{\left(\left(d+s\right)^2+D_1^2\right)^{3/2}} - \frac{3D_1^2}{\left(\left(d+s\right)^2+D_1^2\right)^{5/2}}\right. \\ &\quad \left. + \frac{1}{\left(\left(d-s\right)^2+D_1^2\right)^{3/2}} - \frac{3D_1^2}{\left(\left(d-s\right)^2+D_1^2\right)^{5/2}}\right] \\ &\quad + \lambda\left[\frac{1}{\left(s^2+D_1^2\right)^{3/2}} - \frac{3D_1^2}{\left(s^2+D_1^2\right)^{5/2}}\right. \\ &\quad \left. + \frac{1}{\left(s^2+D_1^2\right)^{3/2}} - \frac{3D_1^2}{\left(s^2+D_1^2\right)^{5/2}}\right]. \end{aligned} \tag{12}$$

To obtain a flat potential well, the potential energy at $x = d$ has to be zero, i.e.

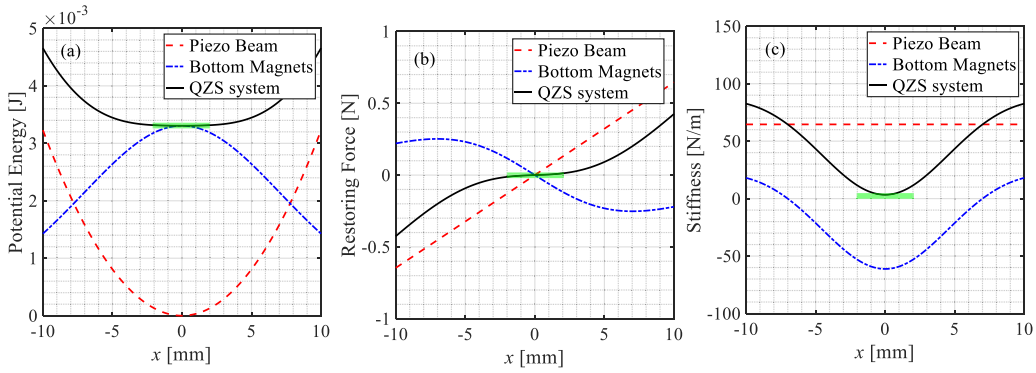

Figure 3. The conventional QZS system: (a) Potential Energy, (b) Restoring Force, (c) Equivalent Stiffness.

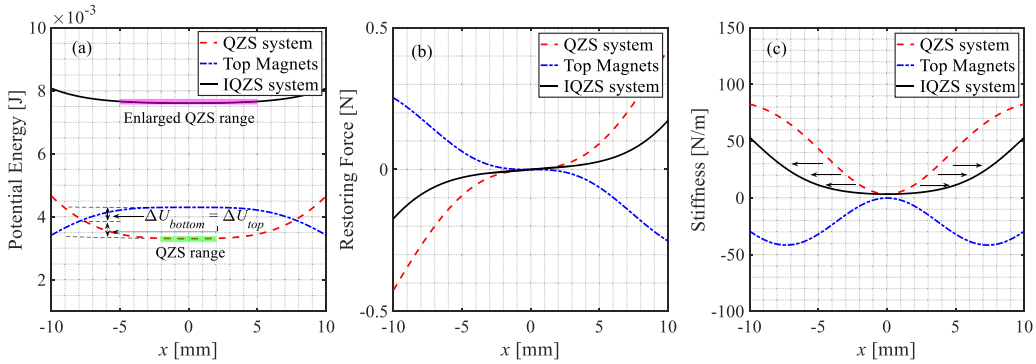

Figure 4. The proposed IQZS system: (a) potential energy, (b) restoring force, (c) equivalent stiffness.

$$\Delta U_{\text{bottom}} + \Delta U_{\text{top}} = 0. \tag{13}$$

In the case of a large d, equation (13) can be used to attain a flat potential well at large displacement (as shown in figure 4(a)). Therefore, based on equation (13), one can carefully tune the magnetic distance D_1 and s to generate a flat potential well over a wide range. Figure 4 compares the potential energy and the equivalent stiffness of the conventional and the proposed IQZ systems. The parameters used for the calculation are listed in table 1. The displacement range in which the equivalent stiffness is below a predefined threshold (k_c, close to zero) is assumed to correspond to the QZS range [26]. In this study, k_c is set to be 10 N m^{-1}. As shown in figures 3 and 4, the QZS range of the conventional system spans from -1.8 mm to 1.8 mm, with a width of 3.6 mm, while that of the proposed IQZS system extends from -4.66 mm to 4.66 mm, with a width of 9.32 mm. These results demonstrate that the proposed method significantly enlarges the QZS range.

3. Analytical solution

3.1. Harmonic balance analysis

To obtain the approximate analytical solutions to the governing equations of the QZS-GPEHs, the HBM is employed. However, due to the complex mathematical form of the magnetic forces, directly applying the HBM is not feasible. To address this issue, the nonlinear magnetic forces are first approximated using a series of polynomial functions,

$$F_m \approx k_1 x + k_3 x^3 + k_5 x^5 \tag{14}$$

where k_1, k_3, and k_5 are the coefficients of fitted restoring forces, respectively. Given the parameters listed in table 1, the restoring forces of the QZS- and IQZS-GPEHs can be computed. The magnet distance of the QZS-GPEH D_0 is set to 15 mm. For the IQZS-GPEH, the three distances are set as $D_0 = D_1 = 15$ mm and $s = 14$ mm. Figure 5 compares the fitted results with the ones calculated using the dipole-dipole model. The results indicated that this fitting approximation offers good accuracy.

Submitting equation (15) back into the original governing equations (equation (8)) gives:

$$\begin{cases} M\ddot{x} + C\dot{x} + k_1 x + k_3 x^3 + k_5 x^5 - \dfrac{1}{2}\rho L D U^2 \left[s_1 \dfrac{\dot{x}}{U} - s_3 \left(\dfrac{\dot{x}}{U} \right)^3 \right] - \theta v = 0 \\ \theta \dot{x} + C_p \dot{v} + \dfrac{v}{R} = 0 \end{cases}. \tag{15}$$

Assume the solutions to equation (15) follow:

$$\begin{cases} x = a \sin \omega t + b \cos \omega t \\ v = a_1 \sin \omega t + b_1 \cos \omega t \end{cases} \tag{16}$$

where ω is the angular frequency of the system, a and b are the structural response constants, a_1 and b_1 are the output voltage constants.

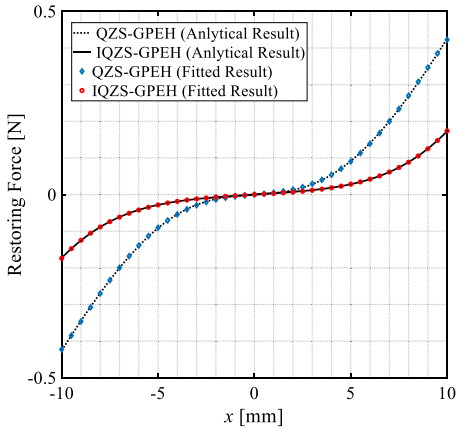

Figure 5. Restoring forces calculated using the dipole-dipole model and their corresponding fitted results for the QZS-GPEH and IQZS-GPEH.

First, substituting equation (16) into the second expression of equation (15) and balancing harmonic terms yields

$$-\theta v = -c_p\dot{x} - k_p x \tag{17}$$

where k_p and c_p are the piezoelectric patch and circuit load-induced electrical stiffness and damping, respectively. They can be further expressed as:

$$\begin{cases} c_p = \dfrac{\theta^2 R}{(C_p\omega R)^2 + 1} \\ k_p = \dfrac{C_p(\theta R\omega)^2}{(C_p\omega R)^2 + 1} \end{cases}. \tag{18}$$

By substituting equations (16)–(18) into the first expression of equation (15), neglecting the high-order harmonics and balancing the harmonic terms, we obtain

$$\begin{cases} \left(k_1 - m\omega^2 + \dfrac{3}{4}r^2k_3 + \dfrac{5}{8}k_5r^4 + k_p\right)b + \left(\omega C - \omega\dfrac{1}{2}\rho LDUs_1 + \dfrac{3}{8U}s_3r^2\omega^3\rho LD + \omega c_p\right)a = 0 \\ \left(k_1 - m\omega^2 + \dfrac{3}{4}r^2k_3 + \dfrac{5}{8}k_5r^4 + k_p\right)a - \left(\omega C - \omega\dfrac{1}{2}\rho LDUs_1 + \dfrac{3}{8U}s_3r^2\omega^3\rho LD + \omega c_p\right)b = 0 \end{cases} \tag{19}$$

where r is the response amplitude of the system, i.e. $r^2 = a^2 + b^2$.

Rearranging equation (19), we have

$$\begin{cases} k_1 - m\omega^2 + \dfrac{3}{4}r^2k_3 + \dfrac{5}{8}k_5r^4 + k_p = 0 \\ C - \dfrac{1}{2}\rho LDUs_1 + \dfrac{3}{8U}s_3r^2\omega^2\rho LD + c_p = 0 \end{cases}. \tag{20}$$

By solving equation (20), the approximate solution of the governing equations can be obtained.

3.2. Numerical verification

To verify the approximate solution, numerical simulations were performed using parameters identified from experiments, summarized in table 1. Two configurations, namely the QZS-GPEH and the IQZS-GPEH, were investigated. Their responses were numerically calculated using the Runge–Kutta method.

It is important to note that the dipole-dipole model was employed to represent magnetic interactions in the numerical simulation, whereas the fitted restoring force was utilized in the analytical solution. Figure 6 presents a comparison between the numerical and analytical results. Firstly, the cut-in wind speed predicted by the analytical solution is approximately 2.89 m s^{-1}, which closely aligns with the numerical result of 2.90 m s^{-1}. This excellent agreement arises primarily because the cut-in wind speeds of the two systems are mainly determined by structural damping and exhibit minor sensitivity to the restoring force. Consequently, the approximation of the restoring force has a negligible impact on the cut-in wind speed in the analytical predictions.

As galloping occurs, both the QZS-GPEH and the IQZS-GPEH conduct limit-cycle oscillations, with the response amplitude increasing monotonically as wind speed rises. It is evident that the analytical predictions are consistently lower than the numerical simulations for both configurations. This discrepancy becomes more pronounced as wind speed

Table 1. Common parameters for the QZS-GPEH and the IQZS-GPEH.

Parameters	Values	Parameters	Values
Effective mass, M [g]	11.71	Height of bluff body, L [m]	0.12
Effective stiffness, K [N m^{-1}]	64.59	Width of bluff body, D [m]	0.035
Damping ratio, ξ	0.0174	Vacuum permeability, μ_0	$4\pi \times 10^{-7}$
Damping, C [N·s m^{-1}]	0.303	Magnetization of magnets M_A, M_B	0.915×10^6
Electromechanical coupling θ, [μN/V]	54.84	Volume of magnets, V_A, V_B [mm^3]	108π
Coefficients of the transverse galloping force, s_1 and s_3	4.34, 86.9	Air density, ρ [kg m^{-3}]	1.225
Coefficients of F_m (QZS-GPEH), k_1, k_3, k_5	4.488 5.988×10^5 -2.212×10^9	Coefficients of F_m (IQZS-GPEH), k_1, k_3, k_5	3.036 9.247×10^4 5.106×10^8

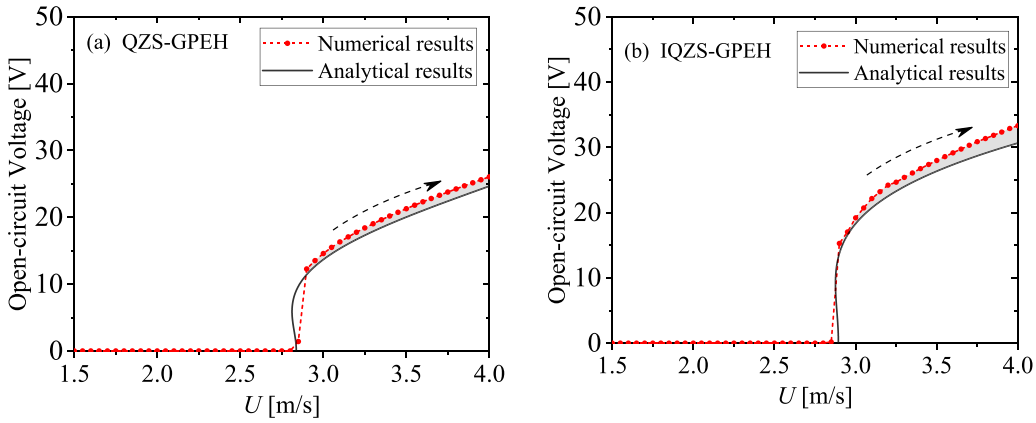

Figure 6. Analytically and numerically calculated open-circuit voltage outputs from the (a) QZS-GPEH, (b) IQZS-GPEH.

increases. For example, the voltage discrepancy of the QZS-GPEH is 1.12 V at $U = 3.3$ m s^{-1} and increases to 1.30 V at $U = 3.6$ m s^{-1}, resulting in an increase of 175.70 mV in the discrepancy. Similarly, for the IQZS-GPEH, the voltage discrepancy between the numerical and analytical results is 1.401 V at $U = 3.3$ m s^{-1} and increases to 1.81 V at $U = 3.6$ m s^{-1}. This discrepancy is likely due to the approximations inherent in the HBM. Specifically, according to equation (16), only the fundamental harmonic is considered in the analytical solution, while higher-order harmonics are neglected, leading to a reduction of the predicted response amplitude. To improve the accuracy of the analytical prediction, it would be reasonable to incorporate higher-order harmonics into equation (16), although this would increase the complexity of the analytical derivation. However, for a quantitative assessment of the potential advantages of the IQZS-GPEH over the conventional QZS-GPEH, such an approximation in equation (16) remains acceptable.

4. Wind energy harvesting performance

4.1. Dynamic responses

To evaluate the potential advantages of the proposed IQZS-GPEH, a comparative analysis was conducted. Figure 7 depicts their dynamic responses versus the wind speed. It is observed that the cut-in wind speeds of these two systems are nearly identical, with $U_{\text{cut-in}} \approx 2.8$ m s^{-1}. This similarity arises because the cut-in wind speed is mainly governed by structural damping rather than stiffness. Once the wind speed exceeds about 2.8 m s^{-1}, both systems exhibit large-amplitude oscillations. Notably, the displacement response of the IQZS-GPEH is significantly larger than that of the QZS-GPEH. For instance, figures 8(a) and (d) compare the displacement responses of the two systems at wind speeds of $U = 3.2$ m s^{-1} and $U = 3.6$ m s^{-1}, respectively. At $U = 3.2$ m s^{-1}, the displacement response of the QZS-GPEH is 7.48 mm, while that of the IQZS-GPEH is 10.25 mm, representing a 37.03%

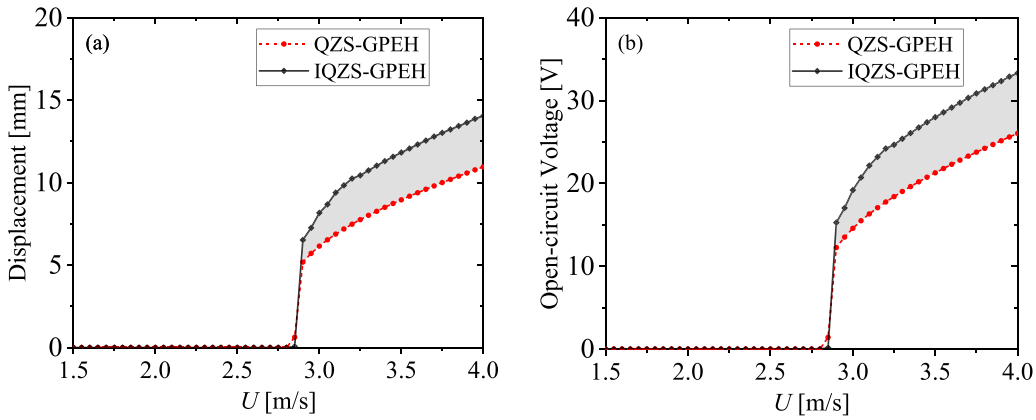

Figure 7. Dynamic responses comparison of QZS-GPEH and IQZS-GPEH: (a) displacement, (b) open circuit voltage.

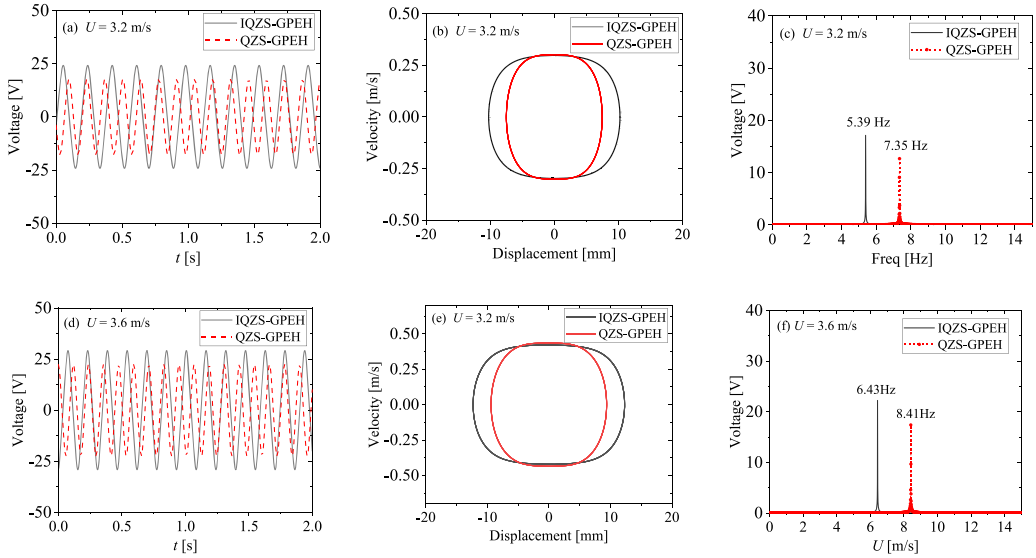

Figure 8. Responses of the QZS-GPEH and IQZS-GPEH at different wind speeds: (a) Open-circuit voltage, $U = 3.2$ m s^{-1}, (b) Phase diagram, $U = 3.2$ m s^{-1}, (c) Frequency spectrum, $U = 3.2$ m s^{-1}, (d) Open-circuit voltage, $U = 3.6$ m s^{-1}, (e) Phase diagram, $U = 3.6$ m s^{-1}, (f) Frequency spectrum, $U = 3.6$ m s^{-1}.

increase. The open-circuit voltages of the QZS-GPEH and IQZS-GPEH are 17.75 V and 25.39 V, respectively, indicating a 43.04% improvement. At $U = 3.6$ m s^{-1}, the displacement response of the QZS-GPEH is 9.39 mm, whereas that of the IQZS-GPEH is 12.31 mm, showing a 31.1% increase. The open-circuit voltages of QZS-GPEH and IQZS-GPEH are 22.30 V and 29.16 V, respectively, corresponding to a 30.76% improvement. Therefore, it can be concluded that the IQZS-GPEH exhibits superior performance compared to the QZS-GPEH at low wind speeds, highlighting its significant potential for enhancing low-speed wind energy harvesting.

Figure 8 compares the open-circuit voltage responses and phase diagrams of the two systems at different wind speeds. For the conventional QZS-GPEH, it generates approximately 17.70 V and 22.30 V at wind speeds of 3.2 m s^{-1} and 3.6 m s^{-1}, respectively. At these same wind speeds, the IQZS-GPEH produces 24.20 and 29.15 V, respectively, demonstrating a significant improvement. Moreover, the phase diagrams in figures 8(b) and (e) reveal that the displacement responses of the IQZS-GPEH are markedly enhanced, while the velocity responses of both systems remain closely matched. According to the governing equation (the second expression of equation (15)), the output voltage is primarily determined by the displacement response for large resistances. In contrast, for small resistances, the velocity has a more dominant effect than the displacement. Therefore, it can be anticipated that the voltage enhancement provided by the IQZS-GPEH will be more pronounced under high load resistance conditions. Besides, the response frequencies of the two systems at $U = 3.2$ m s^{-1} and $U = 3.6$ m s^{-1} are compared in figures 8(c) and (f). It is clearly shown that the IQZS-GPEH exhibits a lower response frequency than the conventional QZS-GPEH, which is attributed to the stiffness reduction resulting from the IQZS configuration.

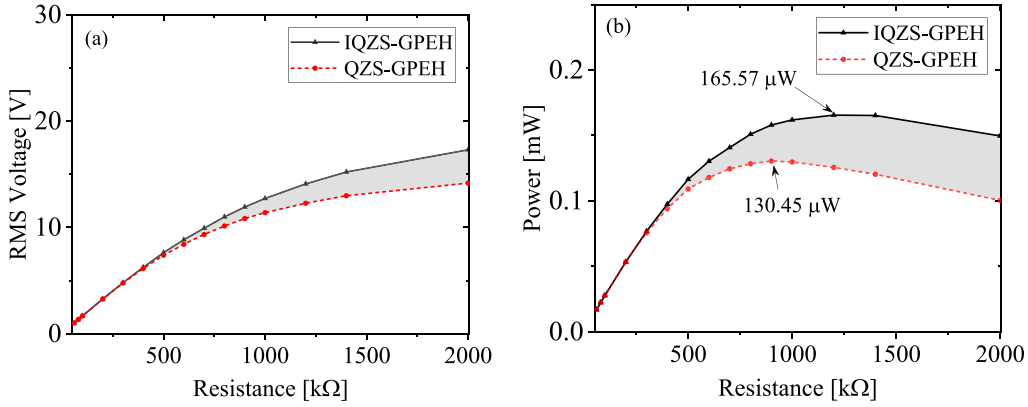

Figure 9. RMS voltage and power of the QZS-GPEH and IQZS-GPEH at $U = 3.6$ m s^{-1}: (a) RMS voltage, (b) Power.

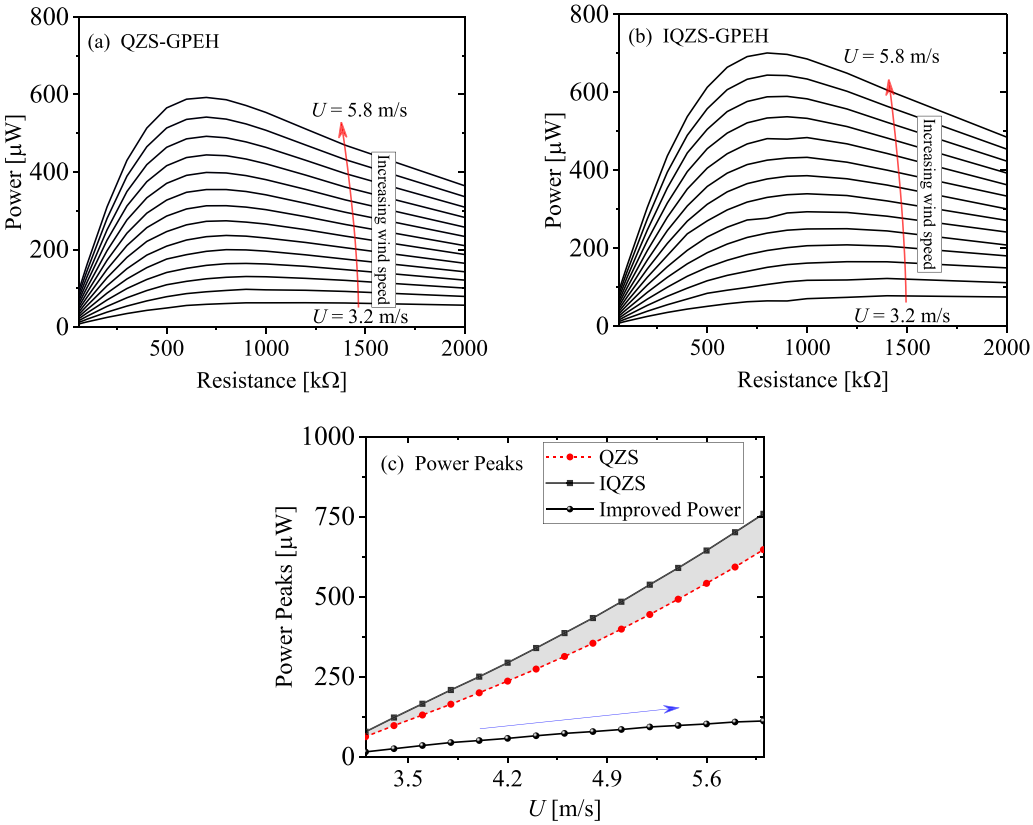

Figure 10. Power outputs of the QZS-GPEH and IQZS-GPEH versus the wind speed U: (a) QZS-GPEH, (b) IQZS-GPEH, (c) peak power amplitudes.

4.2. Power performance

This section compares the power performance of the two systems. Figure 9 illustrates the RMS voltage and power outputs of both systems at a wind speed of $U = 3.6$ m s^{-1}. It is observed that as resistance increases, both the RMS voltage and the voltage difference between the two systems gradually increase. Notably, at small resistance loads, the RMS voltage difference is nearly zero, whereas, at large resistance loads, the IQZS-GPEH generates significantly higher RMS voltage outputs. Similarly, at small resistances, the power outputs of both systems are almost identical, and the IQZS-GPEH delivers higher power output at higher resistances. This observation aligns with the prediction from the structural response comparison in figure 8, which predicted that the advantages of the IQZS-GPEH would become more pronounced at higher resistance loads. Additionally, the peak power of the QZS-GPEH is 130.45 μW, and that of the IQZS-GPEH reaches approximately 165.57 μW, representing a 26.92% improvement.

Subsequently, the influences of wind speed on power outputs are investigated. Figures 10(a) and (b) illustrate the power outputs of the QZS-GPEH and IQZS-GPEH as wind speed increases from 3.0 m s^{-1} to 5.8 m s^{-1} at an increment of 0.2 m s^{-1}. It is evident that for both systems, higher wind

Table 2. Characteristics of the two systems at varying wind speeds.

QZS GPEH	$\boldsymbol{U}$ [m s^{-1}]	**3.2**	**3.4**	**3.6**	**3.8**	**4.0**	**4.2**	**4.4**
	R_{optimal} [kΩ]	1200	900	900	900	800	800	800
	P_{max} [μW]	62.75	97.25	130.45	164.17	199.68	236.29	274.05
	f [Hz]	6.97	7.74	8.27	8.69	9.04	9.33	9.59
	$\boldsymbol{U}$ [m s^{-1}]	**4.6**	**4.8**	**5.0**	**5.2**	**5.4**	**5.6**	**5.8**
	R_{optimal} [kΩ]	800	700	700	700	700	700	600
	P_{max} [μW]	313.13	354.67	398.80	444.13	492.06	541.64	592.43
	f [Hz]	9.81	10.01	10.19	10.35	10.49	10.61	10.73
IQZS GPEH	$\boldsymbol{U}$ [m s^{-1}]	**3.2**	**3.4**	**3.6**	**3.8**	**4.0**	**4.2**	**4.4**
	R_{optimal} [kΩ]	1400	1400	1200	1200	1200	1000	1000
	P_{max} [μW]	78.00	122.5	165.57	208.61	250.23	293.67	339.67
	f [Hz]	4.89	5.67	6.27	6.77	7.19	7.55	7.89
	$\boldsymbol{U}$ [m s^{-1}]	**4.6**	**4.8**	**5.0**	**5.2**	**5.4**	**5.6**	**5.8**
	R_{optimal} [kΩ]	1000	1000	1000	900	900	800	800
	P_{max} [μW]	386.18	433.32	484.10	537.33	589.72	644.17	701.07
	f [Hz]	8.2	8.47	8.74	8.97	9.19	9.38	9.56

speeds result in greater output power. In addition, one notes that the power peak shifts from high resistance to low resistance with increasing wind speed. Figure 10(c) directly plots the peak power amplitudes and power differences between the two systems at various wind speeds. It clearly shows that the IQZS-GPEH generates more power than the conventional QZS-GPEH, with the power enhancement increasing as wind speed rises. For instance, at $U = 3.6$ m s^{-1}, the peak power of the IQZS-GPEH is 165.57 μW, compared to 130.45 μW of the QZS-GPEH, representing a 35.12 μW increase. At $U = 5.0$ m s^{-1}, the peak power of the IQZS-GPEH reaches 484.10 μW, while that of QZS-GPEH is 398.8 μW, indicating an 85.30 μW improvement. Therefore, it has been verified through numerical simulation that expanding the QZS region is an effective method for enhancing the power outputs of QZS-based GPEHs.

Table 2 further reveals the relationships among the optimal resistance, power outputs, and response frequencies of the two systems as the wind speed increases. For both the QZS-GPEH and IQZS-GPEH, the influences of wind speed on power performance follow a similar trend: higher wind speed leads to lower optimal resistance, higher power output, and higher response frequency. For instance, as wind speed increases from 3.2 m s^{-1} to 5.8 m s^{-1}, the optimal resistance of the QZS-GPEH decreases monotonically from 1200 kΩ to 600 kΩ, while that of the IQZS-GPEH decreases from 1400 kΩ to 800 kΩ. At any given wind speed, the optimal resistance of the IQZS-GPEH is consistently higher than that of the conventional QZS-GPEH. Meanwhile, the response frequency of the IQZS-GPEH is consistently lower than that of the QZS-GPEH, which is attributed to the substantial reduction in structural stiffness achieved through the IQZS configuration. Furthermore, for a general galloping energy harvester shunted to a resistive load, its optimal resistance is inversely proportional to the response frequency [27], which explains why the optimal resistance decreases as wind speed increases.

5. Experimental validation

5.1. Experiment setup

The experimental prototype used in this study is shown in figure 11. The aluminum cantilever beam has dimensions of $L_b \times W_b \times H_b = 200$ mm $\times$ 25 mm $\times$ 0.7 mm. The piezoelectric sheet PZT-5 has dimensions of 30 mm $\times$ 20 mm $\times$ 0.4 mm, as illustrated in figure 11(b). Magnets are installed above and below the bluff body. By modifying the number of magnets on the fixture, we can obtain either the QZS-GPEH or the IQZS-GPEH.

The wind tunnel experiments were conducted in a large silent circulating wind tunnel (as shown in figures 11(e) and (f)) with a test section size of 5.5 m $\times$ 1.5 m $\times$ 1.0 m, where the wind velocity nonuniformity is less than 0.5%. The wind speed U is measured using a pitot tube and can be adjusted by varying the frequency f of the draft fan, following the relationship $U = 0.87\,f$—0.038. The experimental setup includes the installation of the prototype in the wind tunnel. The output voltage generated by the prototype is measured using a dual-channel digital oscilloscope (Analog Discovery 2), while the displacement is gauged using a high-resolution laser displacement sensor (SG6150).

Based on the lumped parameter modeling approach for cantilever beam harvesters [28, 29], the equivalent mass can be approximated by the formula $M = (33/140)m_{\text{b}} + m_{\text{t}}$, where m_{b} is the distributed mass of the cantilever beam, and m_{t} is the total mass of the bluff body, tip magnets and 3D printed fixture at the free end. The resonant frequency of the GPEH can be determined by measuring the displacement response. Consequently, the equivalent stiffness K can then be calculated. Then, a free decay test [30] was conducted to determine the damping ratio ξ and structural damping coefficient C. The electromechanical coupling coefficient θ can be determined by measuring the short circuit current at the resonant frequency [28]. All the identified parameters are listed in table 1.

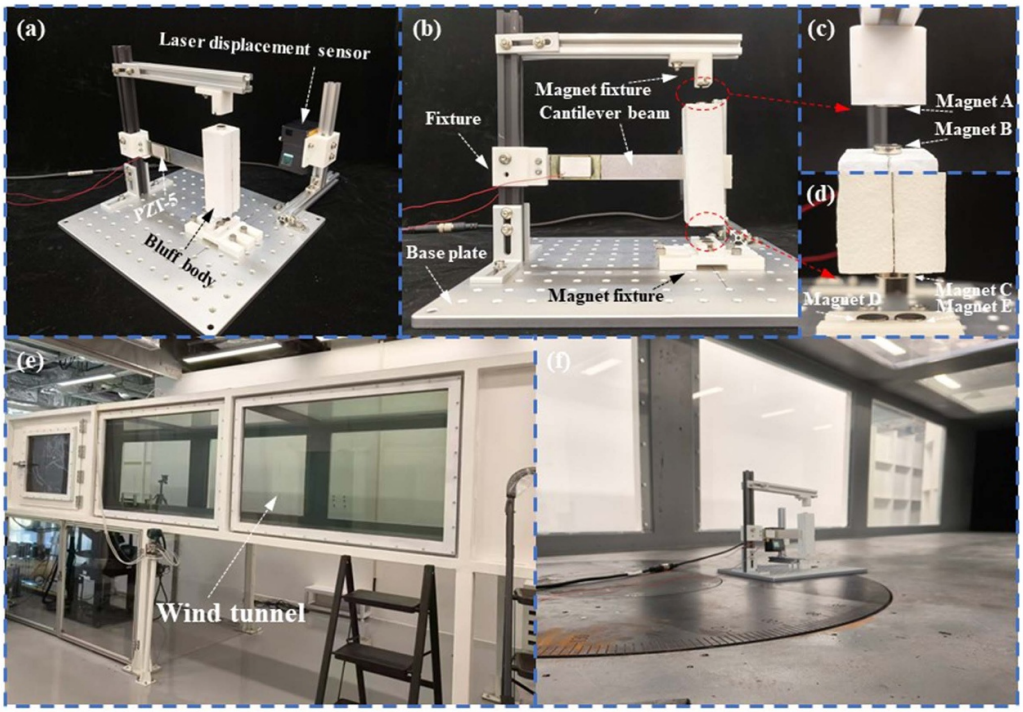

Figure 11. The overview of the experiment setup: (a) the prototyped GPEH; (b) the side view of the GPEH prototype; (c) the enlarged view of the upper magnet configuration; (d) the enlarged view of the lower magnet configuration; (e) the test section of the wind tunnel; (f) the implementation of the GPEH in the wind tunnel.

5.2. Experiment results

Figure 12 shows the open-circuit voltage of the QZS-GPEH and IQZS-GPEH measured in the experiment. It is found that the experimental results agree well with numerical simulations. The cut-in wind speed of the QZS-GPEH identified in the experiment is 2.92 m s^{-1}, which is very close to the numerically predicted result (2.8 m s^{-1}). For the IQZS-GPEH, the experimental cut-in wind speed is 2.746 m s^{-1}, slightly lower than the numerical result of 2.8 m s^{-1}. In the experiment, the cut-in wind speeds of the two systems are slightly different. However, the cut-in wind speeds are almost identical in the numerical simulation. This is because damping is treated as a fixed parameter in the simulation for simplicity. In practice, adjustments to structural stiffness brought by the IQZS configuration may subtly influence the effective damping, resulting in minor variations in cut-in wind speed observed in the experiments.

When the wind speed exceeds the cut-in wind speed, both experimental and numerical results show that the open-circuit voltage of the IQZS-GPEH is higher than that of the conventional QZS-GPEH. For example, at wind speeds of 3.094 m s^{-1}, 3.268 m s^{-1}, 3.442 m s^{-1}, 3.616 m s^{-1}, the open-circuit voltages of the IQZS-GPEH and QZS-GPEH are 17.42 V, 19.16 V, 21.17 V, 22.91 V and 22.15 V, 25.51 V, 28.46 V, 29.89 V, respectively. The corresponding voltage improvements at the four wind speeds are 4.73 V, 6.35 V, 7.29 V, and 6.98 V. All these results validate that the proposed IQZS-GPEH can significantly improve the energy harvesting performance.

Subsequently, the effects of the load resistance on the power outputs at different wind speeds were experimentally investigated. Figure 13 presents the RMS power of both systems at $U = 3.6$ m s^{-1}. As the resistance load increases, the RMS power initially rises to a peak value at a specific resistance and then decreases with further increases in resistance. Notably, the RMS power of the IQZS-GPEH is consistently higher than that of the QZS-GPEH. The relationship between resistance and RMS power for these two systems is in good agreement with numerical simulations.

At small resistance loads, the power difference between the two systems is relatively small. For instance, when $R_L = 100$ kΩ, the RMS power outputs of the QZS-GPEH and IQZS-GPEH at $U = 3.6$ m s^{-1} are 29.51 μW and 44.0 μW, respectively, corresponding to a power difference of approximately 14.49 μW. When R_L increases to 1000 kΩ, their RMS power outputs become 116.15 μW and 145.42 μW, respectively, with the power difference increasing to 29.27 μW. These experimental results firmly validate that the advantage of the IQZS-GPEH becomes more pronounced at higher resistance loads.

As the wind speed increases to 5.0 m s^{-1}, the power characteristics of both systems remain similar, with each displaying a single power peak. But, the proposed IQZS-GPEH consistently generates higher power than the conventional QZS-GPEH. Specifically, at $U = 3.6$ m s^{-1}, the peak power amplitudes of the QZS-GPEH and IQZS-GPEH are 117.70 μW (900 kΩ) and 145.42 μW (1000 kΩ), respectively, with a power improvement of approximately 27.72 mW (23.55%). At $U = 5.0$ m s^{-1}, their peak power amplitudes increase to

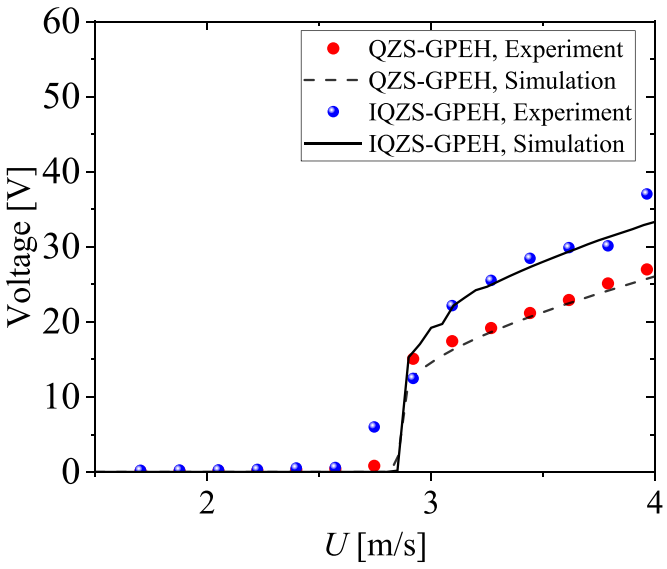

Figure 12. Open-circuit voltage outputs of the QZS-GPEH and IQZS-GPEH versus the wind speed U.

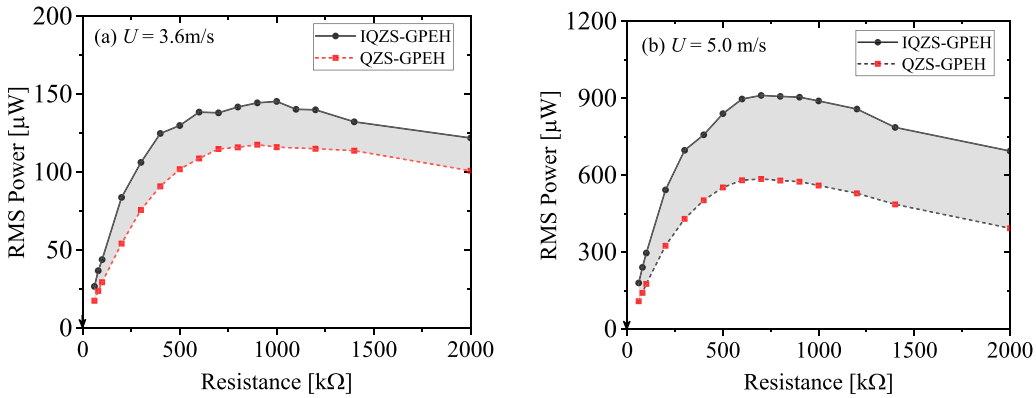

Figure 13. The power outputs of the QZS-GPEH and IQZS-GPEH with the increase of wind speed U: (a) QZS-GPEH, (b) IQZS-GPEH.

585.68 μW (700 kΩ) and 911.54 μW (700 kΩ), respectively, with a power improvement of approximately 325.86 mW (55.64%). The enhanced power generation of the IQZS-GPEH over the QZS-GPEH becomes particularly evident as wind speed increases.

Overall, the experimental results have demonstrated and proven that the proposed IQZS-GPEH significantly improves voltage response and overall energy harvesting performance compared to the conventional QZS-GPEH.

6. Conclusion

This paper has proposed a flat potential-well tuning method and applied it in designing a QZS GPEH. This method allows the QZS property to be extended into the large displacement region, thereby significantly expanding the QZS region. The governing equations of the IQZS-GPEH (IQZS-GPEH) were established, and a static analysis was conducted to showcase the QZS region of the IQZS-GPEH and compare it with that of the conventional QZS-GPEH. The HBM was employed to derive approximate analytical solutions. Numerical simulations were performed to verify the approximate solutions and investigate the dynamics and energy harvesting performance of both systems. Wind tunnel experiments were carried out to validate the results from theoretical analyses and numerical simulations. The key findings are summarized as follows:

(1) It is revealed that the proposed method can effectively enlarge the QZS region, resulting in a significant improvement in dynamic responses and voltage outputs. For example, at $U = 3.6$ m s^{-1}, the open-circuit voltage increased from 22.30 V to 29.16 V, achieving a 30.76% improvement.
(2) The extension of the QZS region can remarkably improve the displacement amplitude while having a minimal impact on the velocity. As a result, the IQZS-GPEH demonstrates a clear energy harvesting advantage over the conventional QZS-GPEH at large resistance loads.
(3) With the wind speed increases, the enhanced power output of IQZS-GPEH also rises. As the wind speed increased

from $U = 3.6\ \mathrm{m\ s^{-1}}$ to $U = 5.0\ \mathrm{m\ s^{-1}}$, the power improvement increased from 23.55% to 55.64%.

In summary, broadening the QZS region is a practical approach to enhancing the performance of QZS-based galloping energy harvesters. The work offers a valuable framework for designing more advanced wind energy harvesting systems.

Data availability statement

All data that support the findings of this study are included within the article (and any supplementary files).

Acknowledgment

This work was financially supported by the National Key Laboratory of Helicopter Aeromechanics (Grant No. 2024-CXPT-GF-JJ-093-04), the Fundamental Research Funds for the Central Universities (Grant No. NT2024002), the National Natural Science Foundation of China (Grant No. 52305135), the Guangdong Provincial Project (Grant No. 2023QN10L545), the Guangzhou Municipal Science and Technology Project (Grant No. 2023A03J0011), the Guangdong Provincial Key Lab of Integrated Communication, Sensing and Computation for Ubiquitous Internet of Things (Grant No. 2023B1212010007), and the Guangzhou Municipal Key Laboratory on Future Networked Systems (Grant No. 024A03J0623).

ORCID iDs

Chunbo Lan https://orcid.org/0000-0001-5959-0488
Ye Zhang https://orcid.org/0009-0008-7316-1792
Yawei Wang https://orcid.org/0000-0002-7041-030X
Guobiao Hu https://orcid.org/0000-0002-1288-7564

References

[1] Priya S and Inman D J 2009 *Energy Harvesting Technologies* (Springer)
[2] Yang Z, Zhou S, Zu J and Inman D 2018 High-performance piezoelectric energy harvesters and their applications *Joule* **2** 642–97
[3] Hu G, Tang L, Liang J, Lan C and Das R 2021 Acoustic-elastic metamaterials and phononic crystals for energy harvesting: a review *Smart Mater. Struct.* **30** 085025
[4] Tan T and Yan Z 2016 Analytical solution and optimal design for galloping-based piezoelectric energy harvesters *Appl. Phys. Lett.* **109** 253902
[5] Shoele K and Mittal R 2016 Energy harvesting by flow induced flutter in a simple model of an inverted piezoelectric flag *J. Fluid Mech.* **790** 582–606
[6] Rostami A and Armandei M 2017 Renewable energy harvesting by vortex-induced motions: review and benchmarking of technologies *Renew. Sustain. Energy Rev.* **70** 193–214
[7] Barrero-Gil A, Alonso G and Sanz-Andres A 2010 Energy harvesting from transverse galloping *J. Sound Vib.* **329** 2873–83
[8] Sirohi J and Mahadik R 2011 Piezoelectric wind energy harvester for low-power sensors *J. Intell. Mater. Syst. Struct.* **22** 2215–28
[9] Sirohi J and Mahadik R 2012 Harvesting wind energy using a galloping piezoelectric beam *J. Vib. Acoust.* **134** 011009
[10] Abdelkefi A, Hajj M and Nayfeh A 2012 Power harvesting from transverse galloping of square cylinder *Nonlinear Dyn.* **70** 1355–63
[11] Zhao L, Tang L and Yang Y 2013 Comparison of modeling methods and parametric study for a piezoelectric wind energy harvester *Smart Mater. Struct.* **22** 125003
[12] Wang J, Zhang C, Gu S, Yang K, Li H, Lai Y and Yurchenko D 2020 Enhancement of low-speed piezoelectric wind energy harvesting by bluff body shapes: spindle-like and butterfly-like cross-sections *Aerosp. Sci. Technol.* **103** 105898
[13] Sun W, Guo F and Seok J 2019 Development of a novel vibro-wind galloping energy harvester with high power density incorporated with a nested bluff-body structure *Energy Convers. Manage.* **197** 111880
[14] Sun W, Jo S and Seok J 2019 Development of the optimal bluff body for wind energy harvesting using the synergetic effect of coupled vortex induced vibration and galloping phenomena *Int. J. Mech. Sci.* **156** 435–45
[15] Bibo A, Alhadidi A and Daqaq M 2015 Exploiting a nonlinear restoring force to improve the performance of flowenergy harvesters *J. Appl. Phys.* **117** 045103
[16] Wang J, Geng L, Zhou S, Zhang Z, Lai Z and Yurchenko D 2020 Design, modeling and experiments of broadband tristable galloping piezoelectric energy harvester *Acta Mech. Sin.* **36** 592–605
[17] Zhao L and Yang Y 2018 An impact-based broadband aeroelastic energy harvester for concurrent wind and base vibration energy harvesting *Appl. Energy* **212** 233–43
[18] Zhao L, Tang L and Yang Y 2014 Enhanced piezoelectric galloping energy harvesting using 2 degree-of-freedom cut out cantilever with magnetic interaction *Jpn. J. Appl. Phys.* **53** 060302
[19] Lan C, Tang L, Hu G and Qin W 2019 Dynamics and performance of a two degree-of-freedom galloping-based piezoelectric energy harvester *Smart Mater. Struct.* **28** 045018
[20] Yang K, Wang J and Yurchenko D 2019 A double-beam piezo-magneto-elastic wind energy harvester for improving the galloping-based energy harvesting *Appl. Phys. Lett.* **115** 193901
[21] Sun W, Jang H and Seok J 2021 Magnetically coupled piezoelectric galloping-based energy harvester using a tandem configuration *Mech. Syst. Signal Process.* **161** 107952
[22] Chen S and Zhao L 2023 A quasi-zero stiffness two degree-of-freedom nonlinear galloping oscillator for ultra-low wind speed aeroelastic energy harvesting *Appl. Energy* **331** 120423
[23] Pan J, Zhang X, Cheng Y, Zhang J and Qin W 2025 Harvesting both wind energy and vibration energy by a zigzag structure with hybrid magnetic and piezoelectric effects *Mech. Syst. Signal Process.* **224** 112066
[24] Chen K, Zhang X, Xiang X, Shen H, Yang Q, Wang J and Litak G 2023 High performance piezoelectric energy harvester with dual-coupling beams and bistable configurations *J. Sound Vib.* **561** 117822
[25] Païdoussis M P, Price S J and Langre E D 2010 *Fluid-Structure Interactions: Cross-Flow-Induced Instabilities* (Cambridge University Press)
[26] Kovacic I, Brennan M J and Waters T P 2008 A study of a nonlinear vibration isolator with a quasi-zero stiffness characteristics *J. Sound Vib.* **315** 700–11

[27] Lan C, Liao Y and Hu G 2022 A unified equivalent circuit and impedance analysis method for galloping piezoelectric energy harvesters *Mech. Syst. Signal Process.* **165** 108339
[28] Tang L and Yang Y 2012 A nonlinear piezoelectric energy harvester with magnetic oscillator *Appl. Phys. Lett.* **101** 094102
[29] Ren M, Wang C, Mohamed M, Yurchenko D, Shu Y and Yang K 2025 Optimization of a comb-like beam piezoelectric energy harvester using the parallel separated multi-input neural network surrogate model *Mech. Syst. Signal Process.* **224** 111939
[30] Leonard M 2007 *Fundamentals of Vibration* (McGraw-Hill)